The scenario of two-dimensional instabilities of the cylinder wake under electrohydrodynamic forcing: a linear stability analysis

2012 Fluid Dyn. Res. 44 055501

(http://iopscience.iop.org/1873-7005/44/5/055501)

IOP PUBLISHING FLUID *DYNAMICS* RESEARCH

Fluid Dyn. Res. **44** (2012) 055501 (20pp) doi:10.1088/0169-5983/44/5/055501

The scenario of two-dimensional instabilities of the cylinder wake under electrohydrodynamic forcing: a linear stability analysis

Juan D'Adamo[1], **Leo M González**[2], **Alejandro Gronskis**[1] **and Guillermo Artana**[1]

[1] Laboratorio de Fluidodinámica, Facultad de Ingeniería, Universidad de Buenos Aires, Argentina
[2] Canal de Ensayos Hidrodinámicos, School of Naval Arquitecture, Universidad Politécnica de Madrid, Spain

E-mail: leo.gonzalez@upm.es

Received 13 July 2011, in final form 15 May 2012
Published 13 June 2012
Online at stacks.iop.org/FDR/44/055501

Communicated by M Asai

Abstract

We propose to study the stability properties of an air flow wake forced by a dielectric barrier discharge (DBD) actuator, which is a type of electrohydrodynamic (EHD) actuator. These actuators add momentum to the flow around a cylinder in regions close to the wall and, in our case, are symmetrically disposed near the boundary layer separation point.

Since the forcing frequencies, typical of DBD, are much higher than the natural shedding frequency of the flow, we will be considering the forcing actuation as stationary.

In the first part, the flow around a circular cylinder modified by EHD actuators will be experimentally studied by means of particle image velocimetry (PIV). In the second part, the EHD actuators have been numerically implemented as a boundary condition on the cylinder surface. Using this boundary condition, the computationally obtained base flow is then compared with the experimental one in order to relate the control parameters from both methodologies.

After validating the obtained agreement, we study the Hopf bifurcation that appears once the flow starts the vortex shedding through experimental and computational approaches. For the base flow derived from experimentally obtained snapshots, we monitor the evolution of the velocity amplitude oscillations. As to the computationally obtained base flow, its stability is analyzed by solving a global eigenvalue problem obtained from the linearized Navier–Stokes equations. Finally, the critical parameters obtained from both approaches are compared.

(Some figures may appear in colour only in the online journal)

0169-5983/12/055501+20$33.00

1. Introduction

It is common knowledge that the non-dimensional parameter determining the behavior of a flow around a cylinder is the Reynolds number $Re = U_o D/\nu$, where U_o is the inflow velocity, D is the cylinder diameter and ν is the kinematic viscosity. The regime that starts when the flow around a cylinder breaks its time continuous invariance at the bifurcation $Re = 48.5$ and exhibits a periodic behavior for limited Reynolds numbers ($Re < 190$) is identified with the Bénard–von Kármán vortex street. In this case, the velocity field in the entire flow domain oscillates with the same global frequency, and a sufficiently large region of absolute instability in the near wake can be identified. Since the oscillation amplitudes depend on the monitored position, the area that contains nonzero oscillation amplitude points, defines the unstable region. Previous studies by Zielinska and Wesfreid (1995) and Wesfreid *et al* (1996) characterized the behavior of this region by determining scale laws for its nonlinear evolution as functions of the Reynolds number.

Global modes evolve with the modification of the base flow external parameters. Barkley (2006) introduced a hypothesis that considers the mean flow of a cylinder wake as the base flow for two-dimensional (2D) stability analysis. Under these conditions, the mean flow represents a marginal stability state and defines the frequency and amplitude of the wake oscillations. The nonlinear saturation of the oscillatory instability is caused by the Reynolds stresses from the modified mean flow. Khor *et al* (2008) and Leontini *et al* (2010) support these hypotheses with experimental and numerical data for Re up to 600. These ideas have been applied to analyze forced wakes. Previous studies on the stability properties of forced wakes by Thiria and Wesfreid (2007, 2009), confirmed that a nonlinear critical behavior takes place under forcing. Indeed, a bifurcation scenario reappears as the forcing action stabilizes the wake fluctuations, in their case, a rotary oscillation. Figure 1, adapted from Thiria and Wesfreid (2007), shows how the reverse flow region quantified by its length L_R varies under forcing. The control actuation, represented by a vertical line for Reynolds numbers above the critical value $Re > Re_c$, varies the reverse flow region when present.

The flow features can be altered by smoothly and accurately varying the forcing parameters to give rise to different regimes. Considering this, we study this problem in order to characterize flow control in wakes by means of electrohydrodynamic (EHD) actuators.

Flow control EHD actuators have received special attention over the last few years, as reviewed by Moreau (2007). Among all types of low-energy plasma actuators, one can notice a group of actuators that produces surface discharges. With these devices, the goal is usually to use the electric *wind* produced by the plasma in order to modify the properties of the boundary layer close to the wall. A particular type of discharge is the surface dielectric barrier discharge (DBD), which was perfected for the first time in air at atmospheric pressure by Masuda and Washizu (1979) for ionic charging of particles. Roth *et al* (1998) used it for airflow applications at the end of the 1990s, characterizing the injected momentum for a flat plate and airfoil flows. Artana *et al* (2003) performed an analysis of the modifications of the recirculation length produced by plasma actuators placed on the cylinder surface following a model proposed by Roshko (1993) for large Reynolds numbers ($Re \sim 10^3$–10^4). Later, Thomas *et al* (2006) applied the DBD in bluff body flow control. With their results, the authors showed drastic reductions in flow separation and the associated Bénard–von Karman vortex shedding. Flows around a cylinder forced with DBD have also recently been studied with the intention of controlling lift forces (Sosa *et al* 2011). Some hypotheses on the dynamics of DBD forcing arose from a computational study validated with PIV experiments in Gonzalez *et al* (2009). In the last work, a finite-element stability analysis (González *et al* 2007) was performed on a bluff body, where vortex shedding was suppressed by a moving surface

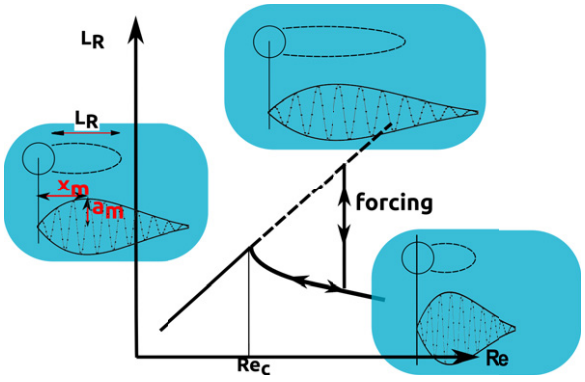

Figure 1. The reverse flow region L_R behind the cylinder evolves nonlinearly with the Reynolds number when the mean flow is modified. The maximum amplitude of the oscillations a_m occurs at $\mathbf{x} = \mathbf{x}_m$ and evolves in a similar manner as in Thiria and Wesfreid (2009). A new bifurcation scenario appears under forcing conditions.

boundary condition. Along these lines, the work of Gronskis (2009), Gronskis *et al* (2009), and other authors (Peers *et al* 2009) analyzed numerical models of DBD forced flows around cylinders at low Reynolds numbers ($Re < 200$).

Our aim in this work is to optimize the DBD control device by analyzing the stability properties of the flow. For this reason, we study the possibility of suppressing vortex shedding when controlling the flow with a DBD actuator. The work has been carried out from both the experimental and the computational point of view. In this context, we pursue the characterization of the DBD control actuator to gain a complete understanding that will eventually lead to more efficient energy consumption.

The work is organized as follows: in section 2, we describe the experimental setup producing the DBD discharge along with the method used for measuring the velocity fields of the flow, in section 3 we detail the characteristics of the problem, boundary conditions and base flow properties, in section 4 the numerical methodology to perform a linear global analysis is described, in section 5 the results obtained by both approaches are shown and compared, and finally, the conclusions and perspectives for future work are presented.

2. The experimental setup

The experimental setup consists of a flow around a circular cylinder at a moderate Reynolds number, $Re \sim 200$. The velocity field measurements were carried out with a cylinder placed in a closed loop wind tunnel, which has a test section of $50 \times 50\,\mathrm{cm}^2$, and an air velocity of $U_o \simeq 0.17\,\mathrm{m\,s}^{-1}$. The cylinder has an external diameter. $D = 20\,\mathrm{mm}$ and a length of 500 mm, giving an aspect ratio of 25 and ensuring that there are no blockage effects.

Quantitative measurements were carried out using 2D particle image velocimetry (PIV) on a vertical plane placed at mid-span of the cylinder. Image acquisition and PIV calculations were performed using a LaVision system, composed of an ImagerPro 1600×1200 CCD camera with a 14-bit dynamic range capable of recording double-frame pairs of images at 8 Hz and a two-rod Nd:YAG (15 mJ) pulsed laser synchronized by a customized PC using LaVision DaVis 7.1 software. The laser sheet width was about 1 mm in the test section. The entire 300 mm $\times$ 200 mm imaging region (about $12 \times 8D$) gives a spatial resolution of $0.06D$

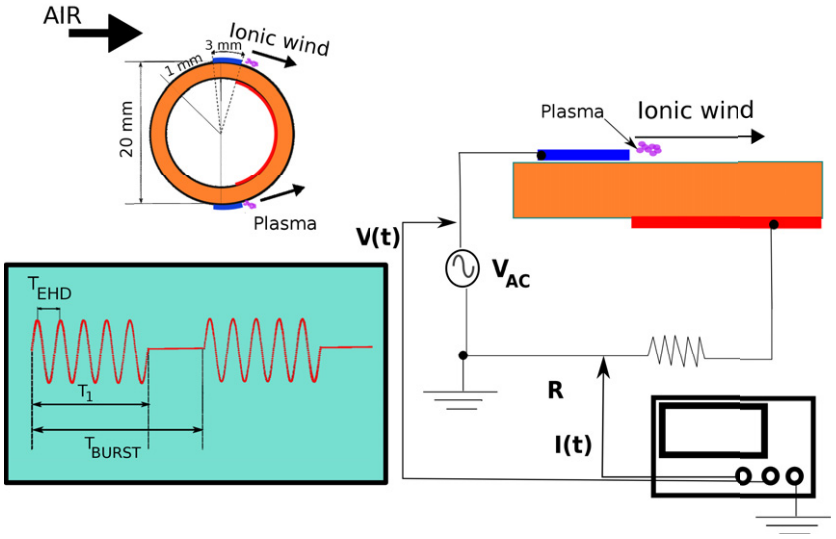

Figure 2. Detailed schematic diagram of the EHD actuator, electric circuit and input signal with the electrodes flush-mounted.

as shown in figure 3. All image acquisitions were done using the double-frame mode with the time lapse between the two frames (dt) set to 700 ms.

From the PIV measurements, we extract the velocity fields from sets of 500 snapshots. The mean velocity fields $\mathbf{u}_{\mathrm{m}}(x)$ and velocity fluctuations $\mathbf{u}'(x)$ are determined as

$$\mathbf{u}_{\mathrm{m}}(\mathbf{x}) = \frac{1}{N}\sum_{i=1}^{N}\mathbf{u}(\mathbf{x}, t_i), \tag{1}$$

$$\mathbf{u}'(\mathbf{x}) = \frac{1}{N}\left[\sum_{i=1}^{N}(\mathbf{u}(\mathbf{x}, t_i) - \mathbf{u}_m)^2\right]^{(1/2)}. \tag{2}$$

This allows us to characterize the incoming free stream flow (U_{o}) from the velocity fluctuation values that are about 5% of U_{o}.

EHD actuators are devices that produce a weakly ionized gas and add momentum to the air flow through collisions of charged particles with the neutral species. Among these devices, a DBD actuator consists of three periodically excited electrodes, two are exposed to the air (represented in blue in figure 2), while the other (represented in red in figure 2) is encapsulated by a dielectric material. The electrical frequencies and voltage required to produce the DBD are typically in the range of kHz and kV.

In our case, the EHD actuator was mounted on both surfaces of a polymethyl methacrylate cylinder tube. As shown in figure 2, the device is composed of an internally embedded electrode, separated from the external electrodes by the 3 mm thick cylinder wall acting as the dielectric barrier. Figure 2 illustrates how the exposed electrodes are positioned on the surface of the cylinder with their plasma generating edges located at 114° with respect to the incoming flow's direction. It was shown via experimental (Thomas *et al* 2006) and numerical (Gronskis 2009) studies that the optimum suppression of vortex shedding occurs close to this position of actuation, which coincides approximately with the boundary layer separation line corresponding to the non-actuated flow.

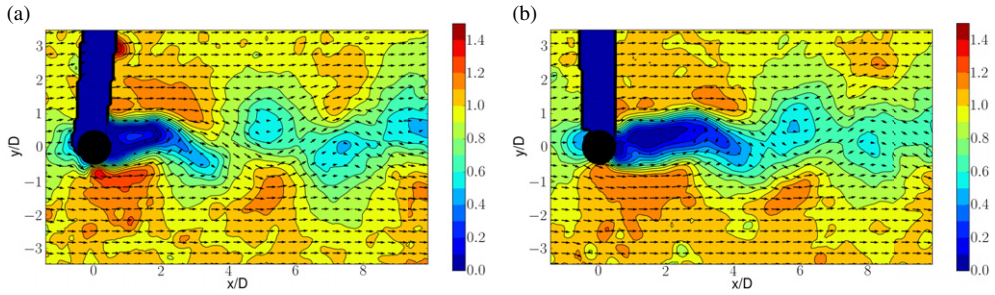

Figure 3. Instantaneous PIV velocity fields under different forcing situations. The region of interest contains 140×86 vectors represented in a coarser grid for better visualization. Contour levels correspond to the velocity modulus. (a) No forcing. (b) Flow under DBD actuation.

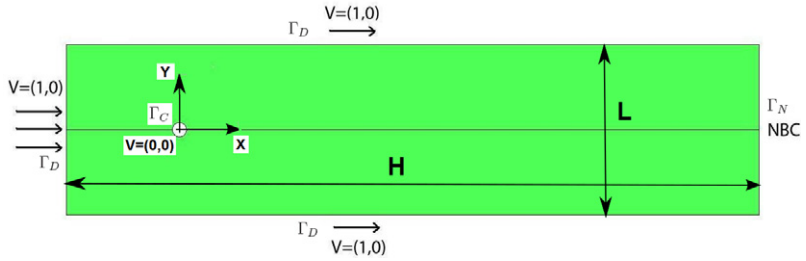

Figure 4. The dimensions, coordinate system and boundary conditions of the computational setup.

The electric circuit, composed of a signal generator, an audio amplifier and an ignition coil, gives a discharge of $V_{\mathrm{EHD}} = 10\,\mathrm{kV}$ and a frequency of $f_{\mathrm{EHD}} = 5.6\,\mathrm{kHz}$. In our experiments these parameters remain fixed. To be able to introduce controlled and moderate actuations, the signal amplitude is modulated by bursting the signal as shown in figure 2. From this, a second frequency arises, $f_{\mathrm{Burst}} = 100\,\mathrm{Hz}$, and the electrical energy delivered by the device is characterized by a duty cycle (DC = T_1/T_{Burst}). Special care was taken to ensure a stationary input since $f_{\mathrm{Burst}} \ll f_{\mathrm{flow}}$, f_{flow} being the vortex shedding frequency. For our experiments, the Strouhal number $St = f\,D/U_{\mathrm{o}} \sim 0.2$, resulting in frequencies $f_{\mathrm{flow}} \sim 1.5\,\mathrm{Hz}$. In short, the flow control parameter in the experimental study is the DC input that modulates the 'ionic wind' amplitude momentum while the forcing can be considered as stationary.

3. Problem definition

The geometry has been non-dimensionalized using the cylinder diameter D as the reference length. The computational geometry is defined by a rectangle with dimensions $L = 20$ and $H = 49$. The center of the cylinder is placed in the middle of the box, eight units behind the inflow boundary, see figure 4.

The plasma actuation takes place in a thin layer compared to the cylinder diameter. This enables us to subdivide the problem into two main regions. An inner region where the forcing occurs and an outer region (where the numerical simulations will be performed) in which electric forces can be disregarded. Therefore, a kinematic compatibility condition can be imposed at the boundary separating both regions. We assume in our case that normal velocity is null and that no discontinuity in tangential velocities exists. We further assume that the law quantifying the tangential velocity distribution is governed by the parameters that determine

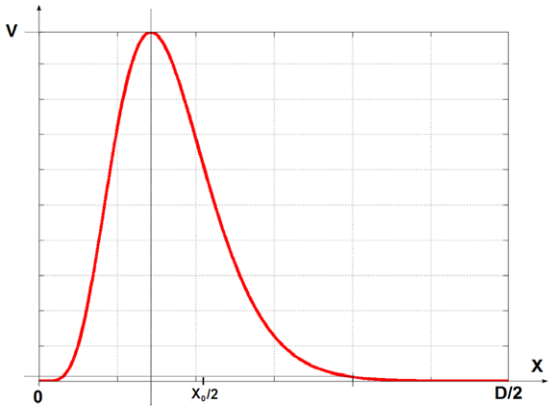

Figure 5. Representation of the velocity magnitude imposed as boundary condition on the cylinder wall when actuation is used ($W = 0.1$ and $x_0 = 0.35$). See equations (3)–(4).

the discharge in the inner region. In this work, no modeling of the inner region based on plasma physics is proposed and the law relating the critical parameters is derived directly from experiments. The boundary condition for the velocity field $\mathbf{V}(\Gamma_C)$ is approximated by the simplified log-normal function (Bermudez *et al* 2010):

$$\mathbf{V}(\Gamma_C) = A e^{f(x)+1-e^{f(x)}} \tau \tag{3}$$

and

$$f(x) = -\frac{2x - x_0}{W}, \tag{4}$$

where x is the horizontal coordinate and varies from 0 to $D/2$, and τ is a tangential unit vector defined as clockwise at the top part of the cylinder and anticlockwise for the bottom part. The boundary velocity $\mathbf{V}(\Gamma_C)$ depends on three parameters: A, W and x_0. A is related to the pulse amplitude, W is related to the pulse width and x_0 is related to the position of the maximum velocity, see figure 5. In the present study, $W = 0.1$ and $x_0 = 0.35$ were fixed according to experimental measurements (Bermudez *et al* 2010) and the influence of the pulse amplitude A was explored as a control parameter.

Thus, for the outer region problem, the boundary can be divided into three parts: Γ_D, composed of the left (inflow), upper and lower boundaries where velocity $V(\Gamma_D) = (1, 0)$ is prescribed; Γ_N, composed of the right (outflow) boundary where natural boundary conditions are used (see equation (8)), and for the cylinder boundary Γ_C, we prescribe a slip velocity imposed by the plasma actuator (numerically representing the thin actuated layer), see equations (3)–(4).

3.1. Base flow calculation

The modifications introduced by the plasma actuator are experimentally measured by the mean flow field variations. These measurements are comprised of 500 snapshots which contain at least 30 shedding periods. Once analyzed through the procedure described later, we observe in figure 6 that the near wake region behind the cylinder enlarges with increasing DC. The streamlines tighten further downstream if a higher EHD actuation is applied,

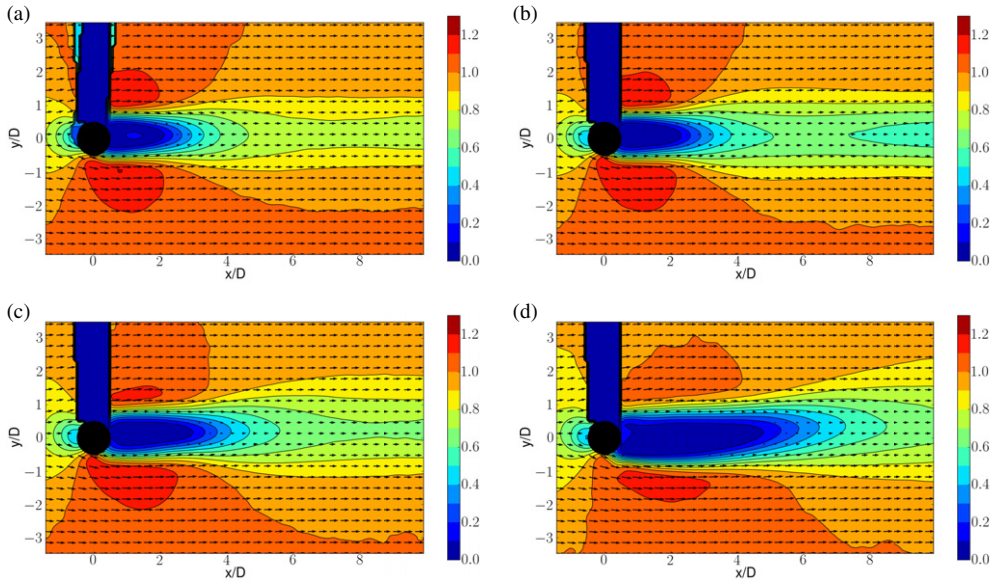

Figure 6. The mean flow velocity vector field and contours of the velocity norm for different values of the DC control parameter.

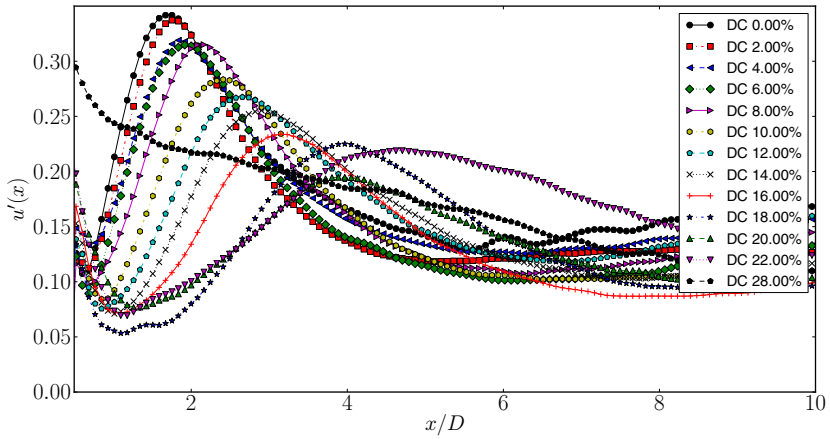

Figure 7. Amplitude of the velocity oscillations u'_x along the horizontal line $y = y_m$ for different values of the DBD forcing parameter (DC).

resulting in the mean flow appearing more like the stationary solution, characterized by a long recirculation zone as shown in figure 1.

The raw data obtained are then computed by a procedure consisting of three main steps. Firstly, we calculate the mean flow with a time average over the total number of experimental snapshots obtained. Secondly, we determine the velocity fluctuations intensity $\mathbf{u}'(\mathbf{x})$ from equation (2). The oscillation amplitude a_m, depicted in figure 1, corresponds to a maximum of $\mathbf{u}'(\mathbf{x})$ located at $\mathbf{x_m} = (x_m, y_m)$. Thirdly, we show in figure 7 the curves resulting from the evaluation of $\mathbf{u}'(\mathbf{x})$ on the horizontal line $y = y_m$. For the non-forced case (DC = 0), we obtain the typical curve associated with a global mode (Wesfreid *et al* 1996). Since the global

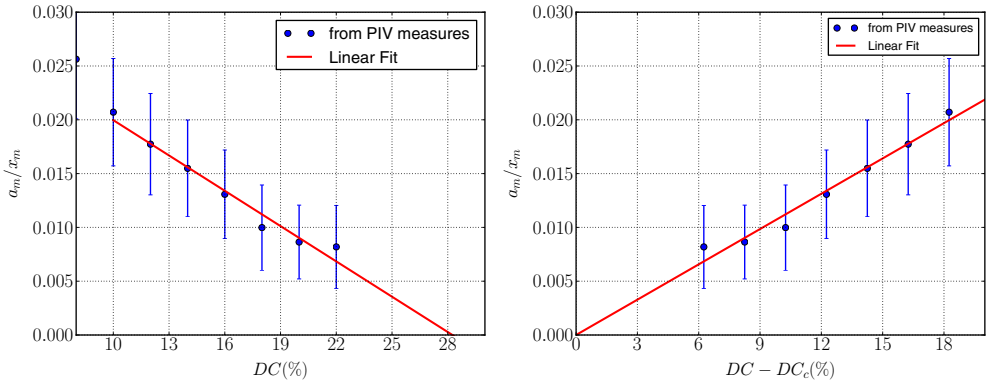

Figure 8. The ratio between the oscillating amplitude a_m and its corresponding horizontal position x_m versus the DC parameter. (a) Determination of the critical value for DC. (b) Given the threshold $\mathrm{DC_c}$, we can extract a scaling law from the evolution of $a_\mathrm{m}/x_\mathrm{m}$.

mode shape changes under forcing, we then plotted the curves that conveniently resume the flow behavior for various values of the DC parameter. We observe that DC increments led to decrements of the a_m and displaced x_m downstream. This scenario is typical of flow stabilization (Thiria and Wesfreid 2009). Above a certain threshold ($\mathrm{DC} = 28$), the global mode is suppressed and the curve changes qualitatively: fluctuations only remain in the cylinder neighborhood. This instability stays confined to a region very close to the wall, typical of convective regimes (Thiria and Wesfreid 2009).

In order to study the global mode evolution, we can further reduce the information by plotting the ratio $a_\mathrm{m}/x_\mathrm{m}$ as shown in figure 8(a). The points from $\mathrm{DC} = 10$ up to $\mathrm{DC} = 22$ can be fitted linearly, allowing us to estimate a critical value $\mathrm{DC_c} \simeq 27.5$. Hence, we can construct a scaling law for (DC–$\mathrm{DC_c}$) presented in figure 8(b).

4. Numerical study

The equations governing incompressible flows are written in primitive-variable formulation as follows:

$$\frac{D\mathbf{u}}{Dt} = -\nabla p + \frac{1}{Re}\nabla^2\mathbf{u} \quad \text{in} \quad \Omega, \tag{5}$$

$$\nabla \cdot \mathbf{u} = 0 \quad \text{in} \quad \Omega, \tag{6}$$

$$\mathbf{u} = \mathbf{V} \quad \text{on} \quad \Gamma_\mathrm{D} \cup \Gamma_\mathrm{C}, \tag{7}$$

$$-p\mathbf{n} + \frac{1}{Re}\nabla\mathbf{u}\cdot\mathbf{n} = 0 \quad \text{on} \quad \Gamma_\mathrm{N}. \tag{8}$$

Here, $\mathbf{u}$ is the velocity field, p is the pressure field, t is the time and ∇ is the nabla operator. The computational domain Ω is limited by the boundaries Γ_D, Γ_C and Γ_N, where Γ_D and Γ_C are the parts of the boundary where the Dirichlet boundary conditions, represented by $\mathbf{V}$, are imposed. The values of $\mathbf{V}$ are described in section 3. Finally, Γ_N is the part of the boundary where the 'natural' boundary conditions (8) are imposed, with $\mathbf{n}$ being the vector normal to the boundary Γ_N. The material derivative operator is defined as usual, $\frac{D}{Dt} = \frac{\partial}{\partial t} + u_j \frac{\partial}{\partial x_j}$, and repeated indices imply summation.

4.1. The steady laminar basic flows

The 2D equations of motion are solved in the laminar regime at appropriate Re values in order to compute steady basic flows $(\mathbf{u}, \bar{p})$ whose stability will subsequently be investigated. The equations read

$$\bar{\mathbf{u}} \cdot \nabla \bar{\mathbf{u}} = -\nabla \bar{p} + \frac{1}{Re} \nabla^2 \bar{\mathbf{u}} \quad \text{in} \quad \Omega, \tag{9}$$

$$\nabla \cdot \bar{\mathbf{u}} = 0 \quad \text{in} \quad \Omega, \tag{10}$$

$$\bar{\mathbf{u}} = \mathbf{V} \quad \text{on} \quad \Gamma_{\mathrm{D}}, \tag{11}$$

$$-\bar{p}\mathbf{n} + \frac{1}{Re} \nabla \bar{\mathbf{u}} \cdot \mathbf{n} = 0 \quad \text{on} \quad \Gamma_{\mathrm{N}}. \tag{12}$$

The values of the boundary field $\mathbf{V}$ are described in section 3. In the solved problem that follows, the basic flow velocity vector is $(\bar{u}_1, \bar{u}_2, 0)$, i.e. its component along the spatial direction x_3 is taken to be zero $\bar{u}_3 = 0$, and all components are taken to be independent of this spatial direction, $\frac{\partial \bar{u}_i}{\partial x_3} = 0$. Consequently, the linearized equations of motion defining the BiGlobal stability problem to be solved may be expressed by real operators, as will be discussed shortly. The basic flow is obtained by time integration of the system (9)–(10) by a semi-Lagrangian second-order finite element solver ADFC (Rodriguez and González 1999), starting from rest and driven by the boundary conditions.

4.2. Linearized problem around the base flow solution

The basic flow is perturbed by a small-amplitude velocity $\tilde{\mathbf{u}}$ and kinematic pressure $\tilde{p}$ perturbations, as follows:

$$\mathbf{u} = \bar{\mathbf{u}} + \varepsilon \tilde{\mathbf{u}} + \text{c.c.}, \qquad p = \bar{p} + \varepsilon \tilde{p} + \text{c.c.}, \tag{13}$$

where $\varepsilon \ll 1$ and c.c. denotes conjugates of the complex quantities $(\tilde{\mathbf{u}}, \tilde{p})$. Substituting into equations (5) and (6), subtracting the basic flow equations (9) and (10) and linearizing, we obtain the equations for the perturbation quantities

$$\frac{\bar{D}\tilde{\mathbf{u}}}{Dt} + \tilde{\mathbf{u}} \nabla \bar{\mathbf{u}} = -\nabla \tilde{p} + \frac{1}{Re} \nabla^2 \tilde{\mathbf{u}}, \tag{14}$$

$$\nabla \cdot \tilde{\mathbf{u}} = 0, \tag{15}$$

with $\frac{\bar{D}}{Dt} = \frac{\partial}{\partial t} + \bar{u}_j \frac{\partial}{\partial x_j}$. The boundary conditions used for this system are

$$\tilde{\mathbf{u}} = 0 \quad \text{on} \quad \Gamma_{\mathrm{D}} \cup \Gamma_{\mathrm{C}}, \tag{16}$$

$$-\tilde{p}\mathbf{n} + \frac{1}{Re} \frac{\partial \tilde{\mathbf{u}}}{\partial n} = 0 \quad \text{on} \quad \Gamma_{\mathrm{N}}. \tag{17}$$

4.3. Eigenvalue problem formulation and solution methodology.

The separability of temporal and spatial derivatives in (14)–(15) allows the introduction into these equations of an explicit harmonic temporal dependence of the disturbance quantities, according to the ansatz

$$\tilde{\mathbf{u}} = \hat{\mathbf{u}}(x, y) \mathrm{e}^{\mathrm{i}\beta z} \mathrm{e}^{-\omega t}, \tag{18}$$

$$\tilde{p} = \hat{p}(x, y) \mathrm{e}^{\mathrm{i}\beta z} \mathrm{e}^{-\omega t}, \tag{19}$$

where a temporal formulation has been adopted, considering β as a real wavenumber parameter, while ω is the complex eigenvalue sought. Substitution into (14) and (15) yields the following:

$$\left\{\bar{u}_j\frac{\partial}{\partial x_j}+\frac{\partial\bar{u}_1}{\partial x}+\mathrm{i}\beta\bar{u}_3-\frac{1}{Re}\left(\frac{\partial^2}{\partial x_j^2}-\beta^2\right)\right\}\hat{u}_1+\hat{u}_2\frac{\partial\bar{u}_1}{\partial y}+\frac{\partial\hat{p}}{\partial x}=\omega\hat{u}_1, \tag{20}$$

$$\left\{\bar{u}_j\frac{\partial}{\partial x_j}+\frac{\partial\bar{u}_2}{\partial y}+\mathrm{i}\beta\bar{u}_3-\frac{1}{Re}\left(\frac{\partial^2}{\partial x_j^2}-\beta^2\right)\right\}\hat{u}_2+\hat{u}_1\frac{\partial\bar{u}_2}{\partial x}+\frac{\partial\hat{p}}{\partial y}=\omega\hat{u}_2, \tag{21}$$

$$\left\{\bar{u}_j\frac{\partial}{\partial x_j}+\mathrm{i}\beta\bar{u}_3-\frac{1}{Re}\left(\frac{\partial^2}{\partial x_j^2}-\beta^2\right)\right\}\hat{u}_3+\hat{u}_1\frac{\partial\bar{u}_3}{\partial x}+\hat{u}_2\frac{\partial\bar{u}_3}{\partial y}+\mathrm{i}\beta\hat{p}=\omega\hat{u}_3, \tag{22}$$

$$\frac{\partial\hat{u}_1}{\partial x}+\frac{\partial\hat{u}_2}{\partial y}+\mathrm{i}\beta\hat{u}_3=0. \tag{23}$$

In the case of a basic flow velocity vector with components $(\bar{u}_1,\bar{u}_2,0)$ present only on the plane normal to the wavenumber vector, it is possible to deduce a real eigenvalue problem, by redefining the out-of-plane velocity component (Theofilis 2003)

$$\breve{u}_3:=\mathrm{i}\hat{u}_3.$$

This converts the system (20)–(23) into one with real coefficients. Defining

$$\alpha_{ii}=\left\{\bar{u}_j\frac{\partial}{\partial x_j}+\frac{\partial\bar{u}_i}{\partial x_i}-\frac{1}{Re}\left(\frac{\partial^2}{\partial x_j^2}-\beta^2\right)\right\},\qquad j=1,2 \tag{24}$$

(no Einstein summation implied for index i), the left-hand side of the system can be represented by the real non-symmetric operator $\mathfrak{A}$ as

$$\mathfrak{A}=\begin{pmatrix}\alpha_{11} & \dfrac{\partial\bar{u}_1}{\partial y} & 0 & \dfrac{\partial}{\partial x}\\[2ex] \dfrac{\partial\bar{u}_2}{\partial x} & \alpha_{22} & 0 & \dfrac{\partial}{\partial y}\\[2ex] 0 & 0 & \alpha_{33} & -\beta\\[2ex] \dfrac{\partial}{\partial x} & \dfrac{\partial}{\partial y} & \beta & 0\end{pmatrix}. \tag{25}$$

A standard finite element variational formulation was used for the system (20)–(23) based on Taylor–Hood elements. The real operator $\mathfrak{A}$ is consequently transformed into its corresponding discrete form, which is represented by a $(3N+NL)\times(3N+NL)$ matrix, where N is the number of velocity nodes and NL is the number of pressure nodes. The right-hand side of the system (20)–(23) is represented by the real symmetric operator $\mathfrak{B}$ introduced by

$$\mathfrak{B}=\begin{pmatrix}M & 0 & 0 & 0\\ 0 & M & 0 & 0\\ 0 & 0 & M & 0\\ 0 & 0 & 0 & 0\end{pmatrix}, \tag{26}$$

where M represents an $N \times N$ mass matrix. The system (20)–(23) is thus transformed into the real generalized eigenvalue problem for the determination of ω,

$$\mathfrak{A}\begin{pmatrix}\hat{u}_1\\ \hat{u}_2\\ \breve{u}_3\\ \hat{p}\end{pmatrix} = \omega\mathfrak{B}\begin{pmatrix}\hat{u}_1\\ \hat{u}_2\\ \breve{u}_3\\ \hat{p}\end{pmatrix}. \tag{27}$$

The real generalized eigenvalue problem (27) has either real or complex solutions, corresponding to stationary ($\omega_i = 0$) or traveling ($\omega_i \neq 0$) modes. The β parameter allows us to analyze the possibility of investigating 3D instabilities ($\beta > 0$). When the β parameter is equal to zero, the operators $\mathfrak{A}$ and $\mathfrak{B}$ are both real and the generalized eigenvalue problem (27) has either real or complex conjugate pairs of solutions. Real arithmetics suffices for the calculation and storage of (and subsequent operations with) the non-zero elements of the matrices $\mathfrak{A}$ and $\mathfrak{B}$.

From a linear stability analysis point of view, the most important eigenvalues are those closest to the axis $\omega_r = 0$, where $\omega_r < 0$ implies an unstable mode and $\omega_r > 0$ implies a stable mode. Specifically, the well-established iterative Arnoldi algorithm has been used for their determination; see González *et al* (2007) for details.

All computations were performed *serially* on a 3.0 GHz Intel P-IV PC. A typical leading dimension of the matrix $\mathfrak{A}$ used in the analyses is $\mathrm{DIM}(\mathfrak{A}) \equiv 3N + NL = O(7 \times 10^4)$, while only the non-zero elements of this matrix, $O(9 \times 10^6)$, and those of its LU decomposition are stored.

5. Results

5.1. Base flow results

The first task is to compare the computational results obtained using the forcing parameter A with the experimental results obtained when varying the DC parameter. The computational base flow calculations were performed running the ADFC code until the stationary condition was obtained, see González *et al* (2007) for details. In those cases where the stationary condition was not satisfied, thus becoming periodic, the base flow was obtained by calculating the time average along the period, see Sipp and Lebedev (2007). In figure 9, the horizontal components of the computationally calculated velocity are shown for $(A, Re) = (0.5, 60)$ and $(A, Re) = (1, 80)$. In both cases, the stationary base flows are represented once no variations are appreciated for the evolution of the flow variables $\mathbf{u}$ and p. If we look at the cylinder perimeter, the maximum actuation area can also be appreciated.

In figure 10, different wake cuts are shown for different pairs of control parameters $A = 1, 1.5, 2$ and $\mathrm{DC} = 6, 12, 30$ at $Re = 235$. For each cut, the computational and average experimental velocities have been compared. In the computational case, the subcritical situation $(A, Re) = (2, 235)$ is stationary and the other two $(A, Re) = (1, 235)$ and $(A, Re) = (1.5, 235)$ were averaged in time to obtain the velocity distribution. As can be appreciated from figure 10, the agreement obtained from the experimental and the computed values is quite reasonable, especially taking into account the simplicity of the boundary control model used for mimicking the effect of the plasma actuator.

For the sake of completeness, the mean velocity profiles are not the only compared data and the frequency variation of the vortex shedding was also compared in the case described in figure 10, see table 1. Similarly to what happened with the mean velocity profiles, it can be observed that the experimental and computational Strouhal numbers, St_{exp} and St_{com}, have

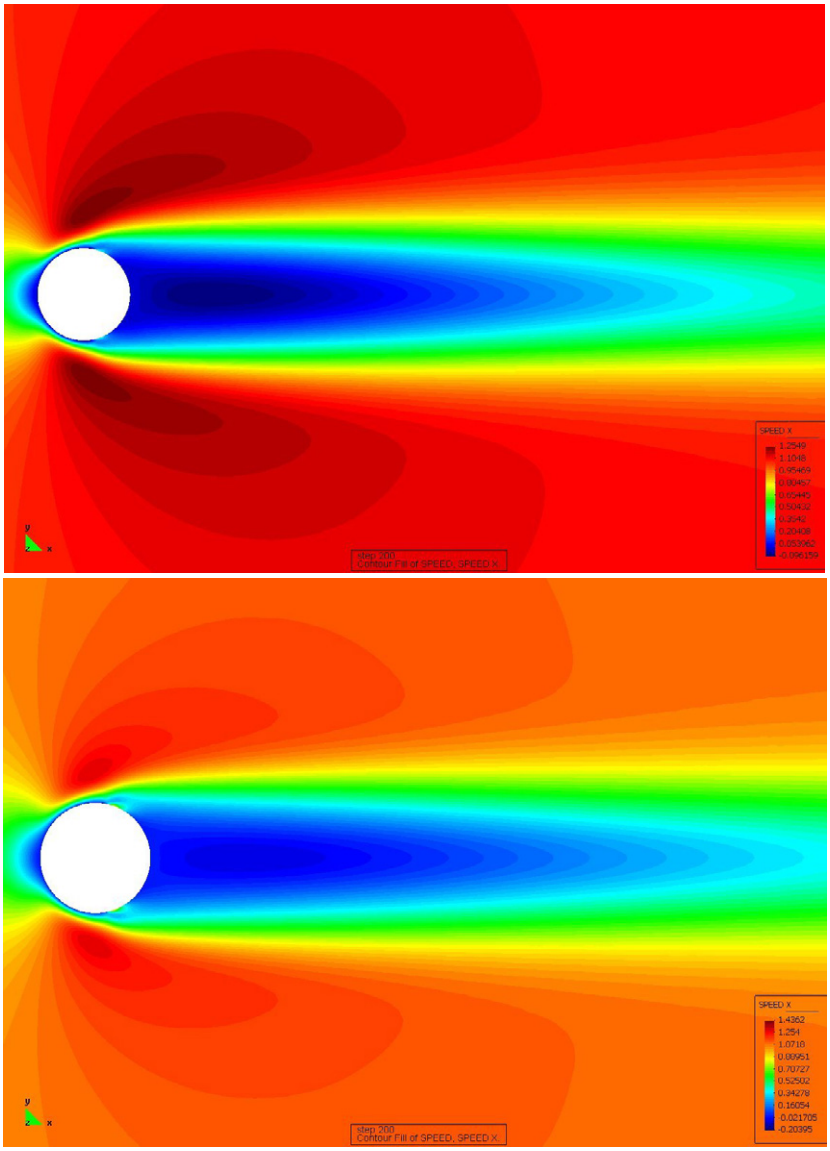

Figure 9. The horizontal component of the stationary base flow velocity field $\bar{u}_1$ for $(A, Re) = (0.5, 60)$ (top) and $(A, Re) = (1, 80)$ (bottom) computed by ADFC.

similar values, validating the computational boundary condition as an appropriate numeric model for the plasma actuator.

In figures 7 and 11, the intensity of the experimental and computational velocity fluctuations has been calculated for different values of the respective control parameters A and DC with the Reynolds number fixed at $Re = 235$ and $y = y_m$. In figure 11, we can appreciate that when the parameter A is increased the fluctuations decrease and the area of maximum fluctuation moves downstream of the cylinder. We can also observe how beyond a certain critical value of the control parameter $A \geqslant 1.9$, the intensity of the velocity fluctuations falls to zero, see figure 11.

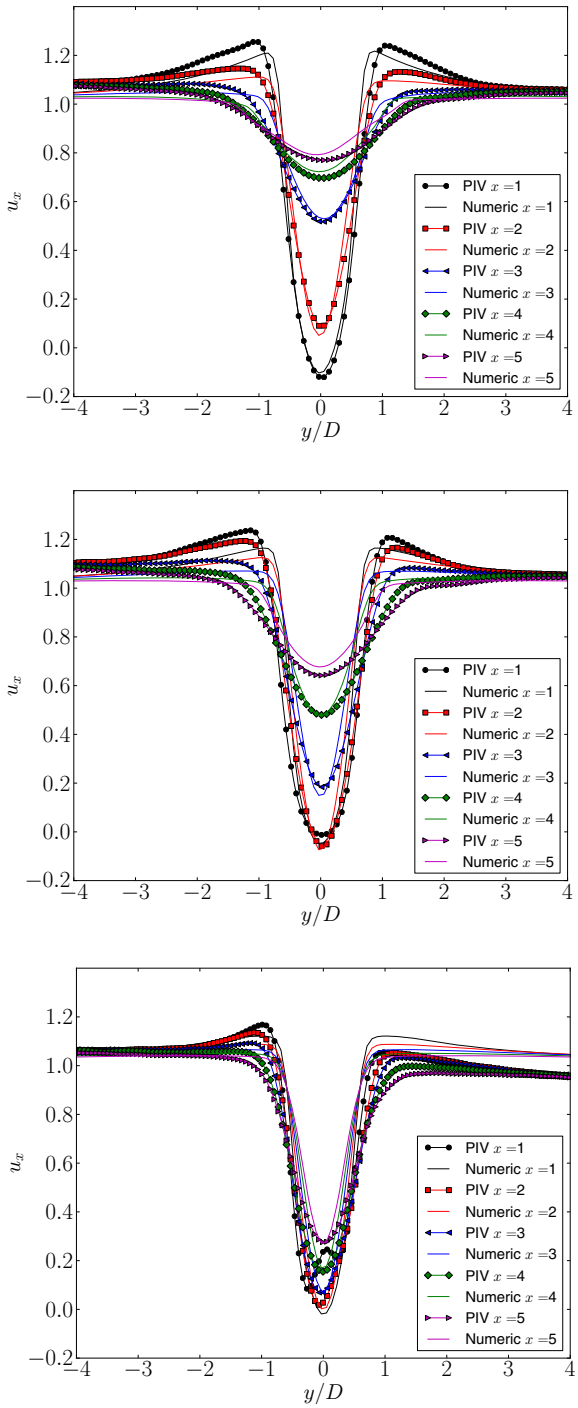

Figure 10. Comparison of the horizontal average velocity profiles at $Re = 235$ for the experimental (dots) and computational (lines) approaches. Three different values of the control parameter are studied: $A = 1$ (top), $A = 1.5$ (middle) and $A = 2$ (bottom). Five wake cuts are shown in each case corresponding to $x/D = 1, 2, 3, 4, 5$.

Table 1. Measured and computed Strouhal numbers corresponding to the shedding frequencies for the compared cases, $Re = 235$ and $A = 1$, 1.5, 2. The uncertainty of the experimental Strouhal numbers is ± 0.02.

Re	A	DC	St_{exp}	St_{com}
235	1	5	0.19	0.194
235	1.5	13	0.13	0.113
235	2	28	0.01	stable

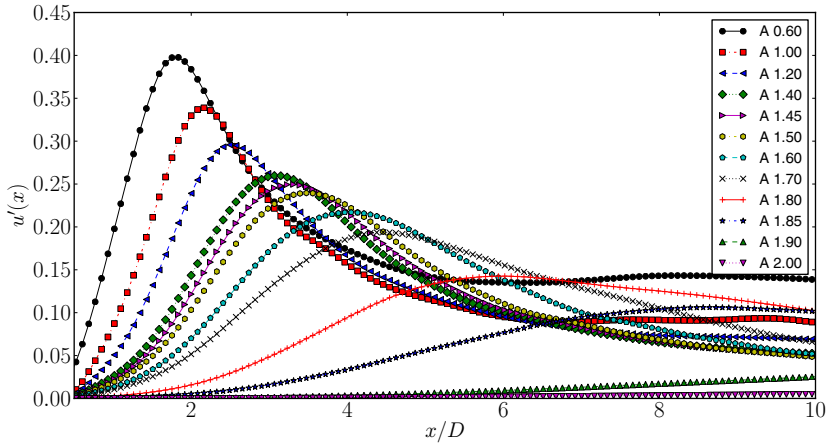

Figure 11. Computational results of the rms of the velocity profiles along the horizontal line $y = y_{\text{m}}$ for $Re = 235$. Each curve represents a different value of the control parameter A varying from 0.6 to 2.

There are different reasons for which the experimental (figure 7) and the computational (figure 11) results do not coincide for $x < 1$. First, the electrodynamic actuation can exhibit a normal component in the immediate vicinity of the exposed edge of the electrode that is not included in the computational model. A second important difference between the numerical simulation and the real EHD actuation is that the implemented boundary condition is completely stationary, while the EHD mechanism corresponds to a high-frequency forcing. Although the wake flow seems to be quite insensitive to high-frequency forcing, the boundary layer could be excited by perturbations having the same frequencies as the modulation used for the actuation. Nonetheless, it is expected that these perturbations stay very localized and their effects remain negligible in the wake area, making the results similar to those produced by the numerical computation. Finally, although the numerical model is in 2D, moderate 3D effects associated with slight non-uniformities of the discharge along the spanwise direction can appear in experiments for the considered Reynolds numbers. These perturbations are very localized and their effects are not observed in the wake area, making the results similar to those produced by the numerical computation.

The efficiency of the control parameter can be evaluated by calculating the rms of the experimental values, see figure 7. The maximum oscillation decreases and moves towards higher x values when the DC parameter is increased. This general tendency is maintained until the highest value of the control parameter DC = 28 is reached for which the structure of the flow changes drastically. We can assume that experimentally, a zero rms flow is not possible due to the intrinsic instability of the perturbed inflow. Therefore, an equivalent criterion to that used in the numerical procedure (sign change of ω_r) for the current experiments is an

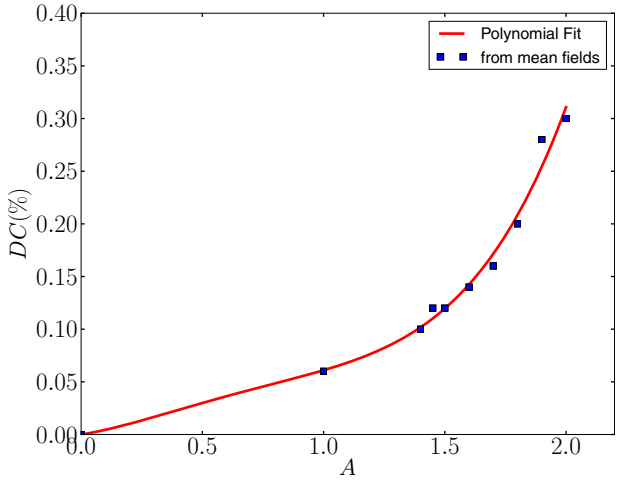

Figure 12. Correlation between the experimental and computational control parameters A and DC.

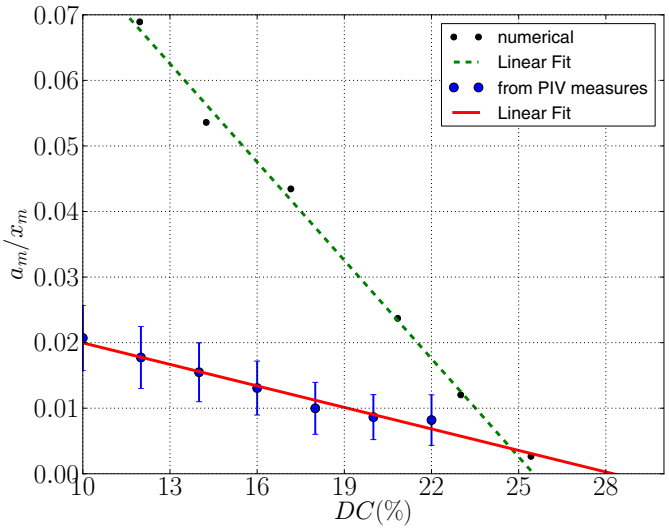

Figure 13. The maximum intensity of velocity fluctuations for the experimental and numerical approaches versus the forcing parameter DC.

abrupt change in the velocity fluctuations field. Hence, for the experimental configuration, we assume that this critical stability threshold is attained when the global mode curves (figure 7) present a drastic change.

Using the comparison results obtained previously, the corresponding values of A and DC are plotted in figure 12. A fourth-order polynomial fitting has been used in order to mathematically correlate both parameters. This picture illustrates one of the most important results of this work where the two control parameters, computational and experimental, are finally related.

Once the control parameters have been related, we can plot the rms evolution for both approaches. In figure 13, the variation of the rms across the entire domain for both approaches

has been plotted using the DC parameter as the reference. As can be observed, the linear fit for both approaches when the rms tends to zero results in a similar critical DC value. The discrepancies between the PIV measurements and the numerical computations in figure 13 are most likely caused by the background turbulence effects. It should be taken into account that the numerical boundary condition assumes certain hypotheses that simplify the most complex aspects of the EHD actuation such as the tangential direction or the space and time distribution of the actuating force. These simplifications may further magnify the differences between both the results.

5.2. Vortex suppression and Hopf bifurcation

As a validation case for the computational stability code, the critical Reynolds number with no acting control was calculated. As was obtained in the paper by Barkley and Henderson (1996), a similar critical Reynolds number $Re = 47$ was obtained here, in excellent agreement with previous studies.

For other flows where the control parameter A is not zero, the value of this parameter has been increased from $A = 0.1$ to $A = 2$. For each combination of the parameters Re and A, the β parameter was varied in the interval $\beta = [0, 10]$ and no 3D instability ($\beta > 0, \omega_r < 0$) was observed. This means that the critical condition is given by a purely 2D disturbance and the flow is less unstable for 3D disturbances. Consequently, in this context, the stability of stationary flows is always produced by the 2D vortex shedding phenomenon, which is analyzed fixing $\beta = 0$. The stability analysis is able to calculate the damping rate and the frequency of a large number of the most unstable modes. In figure 14, the frequency of the least stable mode and the damping rate of that mode have been represented. The base flows used in those subcritical cases were obtained running the ADFC code until the stationary condition was met, while in the supercritical cases, the base flow was obtained by calculating the time average along the period, see Sipp and Lebedev (2007). Two conclusions can be deduced from these figures. Firstly, the frequency of the least stable mode increases when the control parameter is increased, and secondly, the damping rate shows a linear dependence with respect to the Reynolds number when the control parameter is kept constant.

The main result of our investigation is illustrated in figure 15, where the neutral stability curve in the (Re, A) plane has been plotted and the stability regions are distinguishable. The main conclusion inferred from figure 15 is that the plasma control mechanism delays the onset vortex shedding. The effect of the actuator is significant, and small increments of the control parameter A lead to large changes in the critical Reynolds number, with a very sharp increase for $A > 1.5$. In figures 16 and 17, the horizontal and vertical components of the velocity perturbation are shown for $(Re, A) = (65, 0.5)$ and $(Re, A) = (85, 1)$.

It is worth mentioning that another big advantage of the linear stability analysis performed here is that the transition from 2D to 3D flow can easily be studied by changing the value of the $\beta = 2\pi/L_z$ parameter. In all flows close to the critical conditions, the β parameter was varied in the interval $\beta = [0, 10D]$ and no 3D instability was found. This result means that, unlike other similar works on flow control (e.g. Legendre *et al* 2009) where the two-dimensionality of the flow is taken as an assumption, a possible 3D transition is taken into account in our analysis.

The structure of the controlled recirculating flow region and its streamline distribution can be appreciated in figure 18 for the parameter values $(Re, A) = (49, 0.1)$. The dependence of the characteristic length L_R, width S_R and maximum backward velocity u_{max}^{rec} of the recirculating flow region with respect to different critical parameters is studied in table 2.

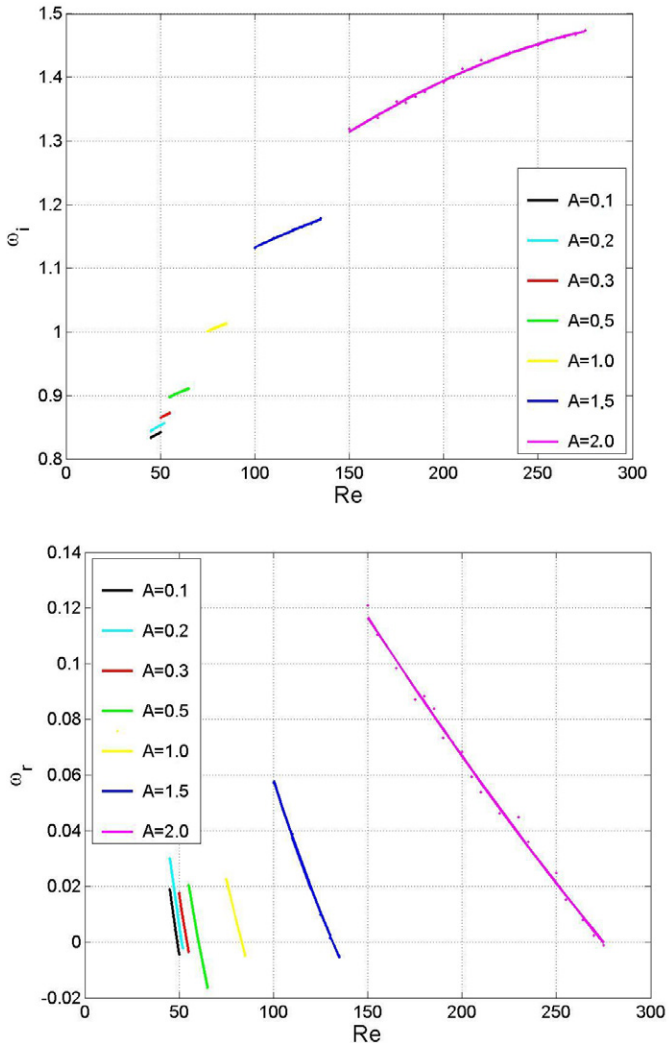

Figure 14. The frequency (top) and damping/growth rate (bottom) of the least stable mode versus the Reynolds number for different values of the control parameter A.

We can deduce from the data in table 2 that the characteristic length of the wake decreases when the critical Reynolds number is increased. Similarly, the width of the wake also narrows when the control parameter A is increased. The critical control situations obtained by simultaneously increasing the Reynolds number and the control parameter A, see figure 15, make the size of the vortex pair (figure 18) behind the cylinder smaller. This actuation has a relevant impact on the maximum horizontal velocity $u_{\max}^{\text{rec}}$ of the wake, which also decreases when the situation requires higher control parameter values.

6. Conclusions

In this work, we performed experimental and direct numerical simulations to study the influence of a plasma actuator on the dynamics of a 2D wake behind a circular cylinder. The

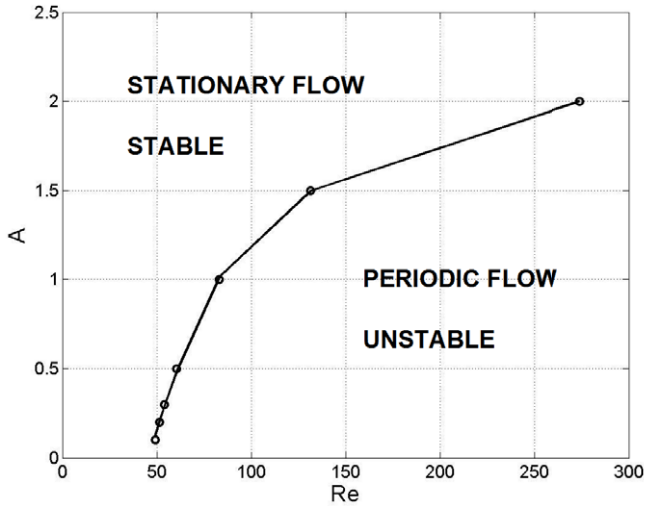

Figure 15. Critical stability curve for the two main parameters: the control parameter A and Reynolds number.

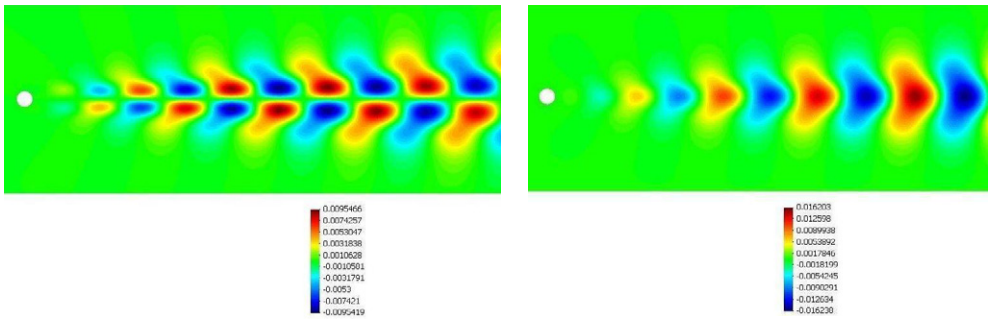

Figure 16. The horizontal (left) and vertical (right) components of the velocity perturbation $\hat{u}_1$ and $\hat{u}_2$ obtained for $A = 0.5$ and $Re = 65$.

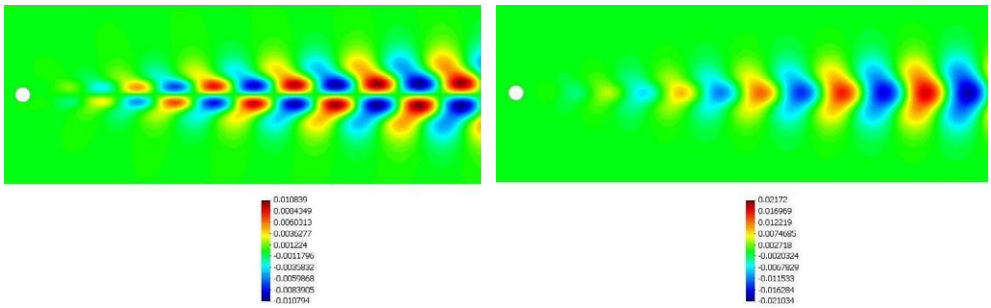

Figure 17. The horizontal (left) and vertical (right) components of the velocity perturbation $\hat{u}_1$ and $\hat{u}_2$ obtained for $A = 1$ and $Re = 85$.

plasma actuation takes place in a thin layer compared to the cylinder diameter. This enables us to subdivide the problem into two regions, a thin inner region where the forcing occurs and an outer region where electric forces can be disregarded. The mathematical law that quantifies the tangential velocity distribution was determined from the experimentally optimized position of

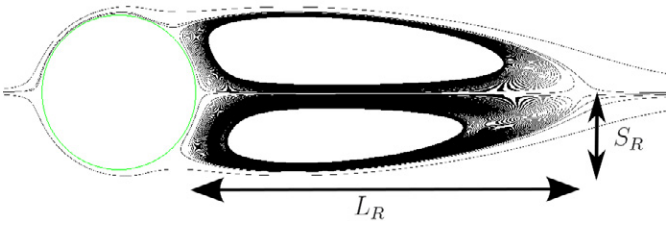

Figure 18. Streamline distribution for a stable case at $Re = 49$ and $A = 0.1$.

Table 2. The characteristic length L_R, width S_R and maximum backward velocity of the cylinder wake for critical values of the A and Re_c parameters.

A	Re_c	L_R	S_R	u_{max}^{rec}
0.1	49.0	2.50	1.02	−0.1176
0.2	51.5	2.44	0.99	−0.1114
0.3	54.1	2.31	0.95	−0.1026
0.5	60.3	2.24	0.86	−0.0961
1	83.1	2.09	0.68	−0.0673
1.5	131.4	2.00	0.58	−0.0463
2	274.8	1.89	0.34	−0.0281

a pair of electrodes. The presence of the plasma control delays the vortex shedding in the wake, makes the recirculation zone longer, alters the vorticity distribution on the cylinder and increases the shedding frequency. The critical values of the control parameters for which the vortex shedding was obtained have been studied as a function of the Reynolds number with a linear stability analysis of the Navier–Stokes equations. The derived generalized eigenvalue problem was solved by an iterative Arnoldi method, thus obtaining the amplitude field, damping rates and frequencies of the dominant modes of the spectrum.

This 3D linear stability approach is also able to predict if the 2D configuration considered as the base flow may develop a 3D instability for any cylinder length. We conclude that in our Reynolds number range no unstable 3D transition of the base flow takes place. It was observed that the actuation at high enough Reynolds values keeps the flow two-dimensional even when the flow without actuation would naturally exhibit a 3D character for these Reynolds numbers.

The neutral stability curve that separates the stable region, where no vortex shedding occurs, from the unstable periodic region has been calculated, and with the performed experiments, good agreement was obtained.

Acknowledgments

We would like to acknowledge the financial support made available by the Universidad Politécnica de Madrid through the Mobility Research Programme UPM-2010. We would also like to thank Mr Hugo Gee for his careful reading of the manuscript.

References

Artana G, Sosa R, Moreau E and Touchard G 2003 Control of the near-wake flow around a circular cylinder with electrohydrodynamic actuators *Exp. Fluids* **35** 580–8

Barkley D 2006 Linear analysis of the cylinder wake mean flow *Europhys. Lett.* **75** 750–6

Barkley D and Henderson R D 1996 Three-dimensional Floquet stability analysis of the wake of a circular cylinder *J. Fluid Mech.* **322** 215–41

Bermudez M M, Sosa R, Grondona D, Márquez A, Kelly H and Artana G 2011 Study of a pseudo-empirical model approach to characterize plasma actuators *J. Phys. Conf. Ser.* **296** 012023

González L, Theofilis V and Gómez-Blanco R 2007 Finite-element numerical methods for viscous incompressible BiGlobal linear instability analysis on unstructured meshes *AIAA J.* **45** 840–55

Gonzalez L M, Artana G, Gronskis A and D'Adamo J 2009 A computational moving surface analogy of an electrodynamic control mechanism in bluff bodies *Global Flow Instability and Flow Control IV (Crete, Greece, September 2009)*

Gronskis A 2009 Modelos numericos para el estudio de flujos externos controlados con actuadores EHD *PhD Thesis* FI UBA pp 1–293

Gronskis A, Sosa R and Artana G 2009 Modeling EHD actuation with slip velocity *Joint ESA/IEEE-IAS/IEJ/SFE/IEA Conference* (Boston, MA) Poster Session 2, paper 2.19 pp 1–6

Khor M, Sheridan J, Thompson M and Hourigan K 2008 Global frequency selection in the observed time-mean wakes of circular cylinders *J. Fluid Mech.* **601** 425–41

Legendre D, Lauga E and Magnaudet J 2009 Influence of slip on the dynamics of two-dimensional wakes *J. Fluid Mech.* **633** 437–47

Leontini J, Thompson M and Hourigan K 2010 A numerical study of global frequency selection in the time-mean wake of a circular cylinder *J. Fluid Mech.* **645** 435–46

Masuda S and Washizu M 1979 Ionic charging of very high resistivity spherical particle *J. Electrost.* **6** 57–67

Moreau E 2007 Airflow control by non thermal plasma actuators *J. Phys. D: Appl. Phys.* **40** 605–36

Peers E, Huang X and Luo X 2009 A numerical model of plasma actuator effects in flow induced noise control *IEEE Trans. Plasma Sci.* **37** 2250–6

Rodriguez A and González L 1999 *ADFC Navier–Stokes Solver* http://adfc.sourceforge.net/

Roshko A 1993 Perspectives on bluff body aerodynamics *J. Wind Eng. Ind. Aerodyn.* **49** 79–100

Roth J, Sherman D and Wilkinson S 1998 Boundary layer flow control with a one atmosphere uniform glow discharge surface plasma *AIAA Meeting (Reno, CV, January 1998)* Paper 98-0328

Sipp D and Lebedev A 2007 Global stability of base and mean-flows: a general approach and its applications to cylinder and open cavity flows *J. Fluid Mech.* **593** 333–58

Sosa R, Artana G, Benard N and Moreau E 2011 Mean lift generation on cylinders induced with plasma actuators *Exp. Fluids* **51** 853–60

Theofilis V 2003 Advances in global linear instability analysis of nonparallel and three-dimensional flows *Prog. Aerosp. Sci.* **39** 249–315

Thiria B and Wesfreid J 2007 Stability properties of forced wakes *J. Fluid Mech.* **579** 137–61

Thiria B and Wesfreid J E 2009 Physics of temporal forcing in wakes *J Fluid Struct.* **25** 654–65

Thomas F, Koslov A and Corke T 2006 Plasma actuators for bluff body flow control *AIAA Meeting (San Francisco, CA, June 2006) Paper 2006-2845*

Wesfreid J, Goujon-Durand S and Zielinska B 1996 Global mode behavior of the streamwise velocity in wakes *J. Physique* II **6** 1343–57

Zielinska B and Wesfreid J 1995 On the spatial structure of global modes in wake flow *Phys. Fluids* **7** 1418